

Time step truncation error in direct simulation Monte Carlo

Alejandro L. Garcia* and Wolfgang Wagner**

* Center for Computational Sciences and Engineering
Lawrence Berkeley National Laboratory, Berkeley, CA 94720
Permanent address: Physics Department, San Jose State University,
San Jose, CA 95192, USA, email: algarcia@wenet.net

** Weierstrass Institute for Applied Analysis and Stochastics
Mohrenstraße 39, D-10117 Berlin, Germany
email: wagner@wias-berlin.de

Abstract. The time step truncation error in direct simulation Monte Carlo calculations is found to be $O(\Delta t^2)$ for a variety of simple flows, both transient and steady state. The measured errors in the transport coefficients (viscosity, thermal conductivity, and self-diffusion) are in good agreement with predictions from Green-Kubo analysis (N. Hadjiconstantinou, *Phys. Fluids*, submitted 1999).

Contents

1. Introduction	2
2. Previous results	3
3. Estimates of Truncation Error	4
4. Simulation Results	8
4.1. Steady state Couette flow (weak gradient)	8
4.2. Steady state Couette flow (strong gradient)	11
4.3. Transient Couette flow	14
4.4. Steady state heat flow (weak gradient)	16
4.5. Steady state heat flow (strong gradient)	18
4.6. Transient heat flow	20
4.7. Steady state tagged particle diffusion	22
5. Concluding Remarks	24
Appendix: Collisionless flow	25
References	27

1. Introduction

The direct simulation Monte Carlo (DSMC) algorithm is a stochastic method that solves the Boltzmann equation by replacing the distribution function with a representative set of particles. As a computational tool, DSMC has been extremely successful in the study of rarefied gas flows, and more recently, for nanoscale problems. We refer to [1] for a tutorial on DSMC and to [4] for a complete reference on the method.

In DSMC the state of the system is given by the positions and velocities of the particles

$$\left\{ \mathbf{r}_i = (x_i, y_i, z_i), \mathbf{v}_i = (v_i^x, v_i^y, v_i^z) \right\}, \quad i = 1, \dots, N.$$

First, the particles are moved as if they did not interact, that is, their positions are updated to

$$\mathbf{r}_i + \mathbf{v}_i \Delta t,$$

where Δt is the **time step**. A particle that reaches a boundary of the system has its position and velocity adjusted according to the imposed boundary condition (e.g., at a periodic boundary the particle's position is replaced with its periodic reflection). Second, after all particles have moved, a given number are randomly selected for collisions. These two steps, **free motion** and **collisions**, are repeated for the desired number of iterations.

Particles are randomly selected as collision partners with the restriction that their mean separation be a fraction of a mean free path. This restriction is enforced by sorting the particles into **cells** and during a time step only permitting collisions among particles in the same cell. The probability of selecting a given pair is a function of the relative speed between the particles, as given by kinetic theory. DSMC evaluates individual collisions stochastically, conserving momentum and energy and selecting the post-collision angles from their kinetic theory distributions. For example, for hard spheres the center of mass velocity and relative speed are conserved in the collision,

$$\mathbf{v}_i^* = \frac{\mathbf{v}_i + \mathbf{v}_j}{2} + \mathbf{e} \frac{\|\mathbf{v}_i - \mathbf{v}_j\|}{2}, \quad \mathbf{v}_j^* = \frac{\mathbf{v}_i + \mathbf{v}_j}{2} - \mathbf{e} \frac{\|\mathbf{v}_i - \mathbf{v}_j\|}{2},$$

with the direction \mathbf{e} of the relative velocity uniformly distributed in the unit sphere. The “no time counter” (NTC) method is used to determine the number of collisions that occur in each cell during a time step.

The algorithm depends on three numerical parameters – the number of simulation particles N , the cell size Δx , and the time step Δt . The behaviour of the DSMC algorithm for $N \rightarrow \infty$ was investigated in [12], where convergence to a discretized version of the Boltzmann equation was established. The problem of cell size dependence was considered in [2], where it was shown that the truncation error in the transport coefficients was $O(\Delta x^2)$ with explicit expressions obtained for the viscosity and thermal conductivity.

The **purpose of this paper** is to study effects of the time step on the accuracy of the computed quantities, and to illustrate second order of the time step error. In Section 2 we recall some theoretical results from the literature. In Section 3 we introduce some test configurations for measuring the time step error. In Section 4 results of numerical experiments are presented. Finally, some concluding remarks are given.

2. Previous results

The **Boltzmann equation** for monoatomic rarefied gases has the form

$$\frac{\partial}{\partial t} f(t, \mathbf{r}, \mathbf{v}) + (\mathbf{v}, \nabla_{\mathbf{r}}) f(t, \mathbf{r}, \mathbf{v}) = \int_{\mathcal{R}^3} d\mathbf{w} \int_{\mathcal{S}^2} d\mathbf{e} B(\mathbf{v}, \mathbf{w}, \mathbf{e}) \left[f(t, \mathbf{r}, \mathbf{v}^*) f(t, \mathbf{r}, \mathbf{w}^*) - f(t, \mathbf{r}, \mathbf{v}) f(t, \mathbf{r}, \mathbf{w}) \right] \quad (2.1)$$

with some initial condition $f(0, \mathbf{r}, \mathbf{v}) = f_0(\mathbf{r}, \mathbf{v})$. The collision transformation is defined as

$$\mathbf{v}^* = \frac{\mathbf{v} + \mathbf{w}}{2} + \mathbf{e} \frac{\|\mathbf{v} - \mathbf{w}\|}{2}, \quad \mathbf{w}^* = \frac{\mathbf{v} + \mathbf{w}}{2} - \mathbf{e} \frac{\|\mathbf{v} - \mathbf{w}\|}{2}, \quad \mathbf{e} \in \mathcal{S}^2,$$

where \mathcal{S}^2 denotes the unit sphere. The hard spheres collision kernel has the form

$$B(\mathbf{v}, \mathbf{w}, \mathbf{e}) = \text{const} \|\mathbf{w} - \mathbf{v}\|.$$

Here we mention some results concerning the convergence behaviour of various stochastic particle schemes related to the Boltzmann equation (see also [13], [10] and references therein).

Convergence of the **DSMC algorithm** with respect to the number of particles was studied in [12]. The limiting behaviour of the particle system is described by a discretized version of the Boltzmann equation consisting of an equation related to the free flow step,

$$\begin{aligned} \frac{\partial}{\partial t} f_k^{(1)}(t, \mathbf{r}, \mathbf{v}) + (\mathbf{v}, \nabla_{\mathbf{r}}) f_k^{(1)}(t, \mathbf{r}, \mathbf{v}) &= 0, \\ f_k^{(1)}(t_k, \mathbf{r}, \mathbf{v}) &= f_{k-1}^{(2)}(t_k, \mathbf{r}, \mathbf{v}), \quad k = 1, 2, \dots, \\ f_0^{(1)}(0, \mathbf{r}, \mathbf{v}) &= f_0(\mathbf{r}, \mathbf{v}), \end{aligned} \quad (2.2)$$

and an equation related to the collision step

$$\begin{aligned} \frac{\partial}{\partial t} f_k^{(2)}(t, \mathbf{r}, \mathbf{v}) &= \int_D d\mathbf{r}' \int_{\mathcal{R}^3} d\mathbf{w} \int_{\mathcal{S}^2} d\mathbf{e} h(\mathbf{r}, \mathbf{r}') B(\mathbf{v}, \mathbf{w}, \mathbf{e}) \\ &\quad \left[f_k^{(2)}(t, \mathbf{r}, \mathbf{v}^*) f_k^{(2)}(t, \mathbf{r}', \mathbf{w}^*) - f_k^{(2)}(t, \mathbf{r}, \mathbf{v}) f_k^{(2)}(t, \mathbf{r}', \mathbf{w}) \right], \\ f_k^{(2)}(t_k, \mathbf{r}, \mathbf{v}) &= f_k^{(1)}(t_{k+1}, \mathbf{r}, \mathbf{v}). \end{aligned} \quad (2.3)$$

The functions $f_k^{(1)}, f_k^{(2)}$ are defined on the time intervals $[t_k, t_{k+1}]$, where $t_k = k \Delta t$. The computational domain (position space) is $D \subset \mathcal{R}^3$. The function h depends on the cell structure and tends to the Dirac function when the cell size Δx tends to zero.

For the **Nanbu algorithm** and some of its modifications the limiting behaviour of the particle system for large particle numbers was established in [3]. Similar equations occur with the only difference that at the right-hand side of (2.3) the t is replaced by t_k . This is due to the fact that recollisions are excluded.

This apparently harmless change of the equation related to the collision step has an important consequence for the time step error of the stochastic particle scheme. Due to

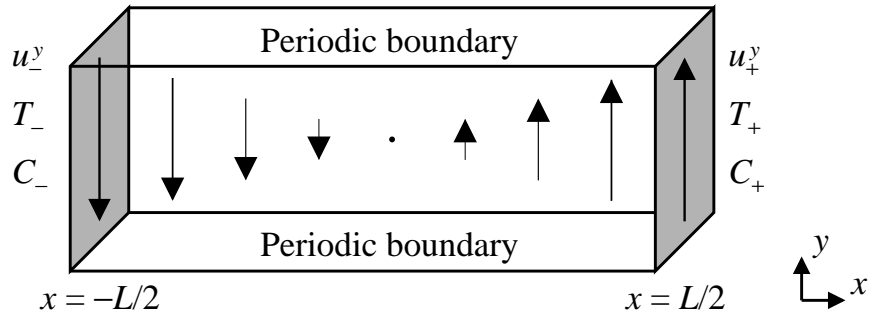


Figure 1: Schematic illustrating the system geometry.

a result from [5], the solutions of the system of equations (2.2), (2.3) approximate the solution to the Boltzmann equation (2.1) with the order $O(\Delta t^2)$ (for vanishing cell size). Thus, the time step error is expected to be of second order for DSMC, while it is only of first order for Nanbu's scheme (see also [7, Ch.10, p.290]). In the steady state case we are not aware of any similar theoretical results concerning the time step error.

Recently it has been claimed [11] that the result from [5] is incorrect. We will investigate the problem of time step error numerically, both in the transient and in the steady state case. Note that convergence of the stationary distribution of the DSMC particle system (without time splitting) to a mollified stationary Boltzmann equation was studied in [6].

3. Estimates of Truncation Error

This section describes the various simulations that were performed and the different functionals that were measured to estimate the time step truncation error.

The system we consider is rectangular with length L , volume V and cross-section $A = V/L$ (see **Figure 1**). The boundary conditions at $x = \pm L/2$ are thermal walls with fixed temperatures T_{\pm} and y -velocities u_{\pm}^y . A particle that strikes a thermal wall has its velocity replaced with a random value generated from the biased Maxwell-Boltzmann distribution in the frame of reference of the wall. Particles that strike a wall are marked as **tagged** ($C_i = 1$) with probability C_{\pm} , and **untagged** ($C_i = 0$) with probability $1 - C_{\pm}$. Dynamically the tagged and untagged particles are identical. The boundaries in the other directions are taken to be periodic. We will study three problems,

- Couette flow ($u_+^y \neq u_-^y$, $T_+ = T_-$, $C_+ = C_-$),
- heat flow ($u_+^y = u_-^y$, $T_+ \neq T_-$, $C_+ = C_-$), and
- tagged particle diffusion ($u_+^y = u_-^y$, $T_+ = T_-$, $C_+ \neq C_-$).

The transport of the fundamental conserved quantities (momentum, energy, and mass) may be measured in these flows.

The system contains N hard sphere particles of mass m and diameter σ . The mean free path for hard spheres is $\lambda = (\sqrt{2}\pi\sigma^2n)^{-1}$, where n is the number density; λ_0 is the

reference mean free path at the reference density $n_0 = N/V$. At the reference temperature, T_0 , the most probable thermal speed is $\bar{v}_0 = \sqrt{2kT_0/m}$, which we use to define the reference time $t_0 = \lambda_0/\bar{v}_0$.

We introduce three sets of functionals measured in the simulations. One set is related to momentum, the others to energy and concentration.

The first **momentum functional** is

$$F_{1\pm}^v = \frac{1}{A(t_f - t_i)} \sum_{\text{impacts}} \left[(mv_i^y)' - mv_i^y \right]$$

where the sum is over all particle impacts with the wall at $\pm L/2$ during the time interval $[t_i, t_f]$; the unprimed and primed denote before and after the particle's impact with the wall. The functional $F_{1\pm}^v$ is the time-averaged change in momentum per unit area for particles striking a wall, which, by the momentum-impulse theorem, gives the **drag force per unit area** on the wall. The viscosity of the gas may be defined as the ratio of this force to the velocity gradient so $F_{1\pm}^v$ is directly related to this transport coefficient. Formally, this functional is defined as

$$F_{1\pm}^v = \frac{1}{A(k_f - k_i)\Delta t} \sum_{k=k_i}^{k_f} \sum_{i=1}^N \left[(mv_i^y)' - mv_i^y \right] H(-L/2 \pm (x_i + v_i^x \Delta t)) \quad (3.1)$$

where $k_i = t_i/\Delta t$ is the first iteration for which statistics are measured and $k_f = t_f/\Delta t$ is the total number of iteration steps. The Heaviside step function H selects those particles that strike the thermal wall at $x = \pm L/2$ during iteration k .

The **second functional** is

$$F_2^v = \frac{1}{A(t_f - t_i)} \sum_{\text{cross}} mv_i^y \text{sign}(v_i^x)$$

where the sum is over all particles that cross the plane $x = 0$. Formally, this may be written as

$$F_2^v = \frac{1}{A(k_f - k_i)\Delta t} \sum_{k=k_i}^{k_f} \sum_{i=1}^N mv_i^y \left[H(-x_i)H(x_i + v_i^x \Delta t) - H(x_i)H(-x_i - v_i^x \Delta t) \right]. \quad (3.2)$$

This functional is the **parallel momentum flux per unit time** and its ratio with the velocity gradient gives the viscosity.

Because momentum is conserved in collisions, the functionals $F_{1\pm}$ and F_2 are closely linked. At the steady state the momentum flux must be constant across the system so $F_{1+}^v = F_{1-}^v = F_2^v$ as $\Delta x \rightarrow 0$, $\Delta t \rightarrow 0$, and $t_f \rightarrow \infty$.

The **third functional** is the y -component of the average fluid velocity extrapolated to the thermal wall boundaries

$$F_{3\pm}^v = \lim_{x \rightarrow \pm L/2} u^y(x). \quad (3.3)$$

This **fluid velocity** is measured in cells as

$$u^y(x) = \frac{\langle v_i^y \rangle}{\langle 1 \rangle}. \quad (3.4)$$

For the **steady state calculations**, the average cell sum of some quantity $Q(\mathbf{v}_i)$ is defined as

$$\langle Q(\mathbf{v}_i) \rangle = \frac{1}{k_f - k_i} \sum_{k=k_i}^{k_f} \sum_{i=1}^N Q(\mathbf{v}_i) H(x_i - (x - \frac{1}{2}\Delta x)) H((x + \frac{1}{2}\Delta x) - x_i) \quad (3.5)$$

with statistical samples taken at the conclusion of each iteration starting with iteration k_i and ending with k_f . The Heaviside functions serve to select the particles in a cell centered between $x - \frac{1}{2}\Delta x$ and $x + \frac{1}{2}\Delta x$. For the **transient calculations**, the average cell sum is defined as

$$\langle Q(\mathbf{v}_i) \rangle = \frac{1}{N_e} \sum_{k=1}^{N_e} \sum_{i=1}^N Q(\mathbf{v}_i) H(x_i - (x - \frac{1}{2}\Delta x)) H((x + \frac{1}{2}\Delta x) - x_i) \quad (3.6)$$

where N_e is the number of runs averaged together in the ensemble and statistical samples are only taken on the last iteration of each run in the ensemble.

We define three **energy functionals** similar to those defined above for momentum. The first is (cf. (3.1))

$$F_{1\pm}^e = \frac{1}{A(k_f - k_i)\Delta t} \sum_{k=k_i}^{k_f} \sum_{i=1}^N \left[\left(\frac{1}{2} m \mathbf{v}_i^2 \right)' - \frac{1}{2} m \mathbf{v}_i^2 \right] H(-L/2 \pm (x_i + v_i^x \Delta t)) \quad (3.7)$$

and the second functional is (cf. (3.2))

$$F_2^e = \frac{1}{A(k_f - k_i)\Delta t} \sum_{k=k_i}^{k_f} \sum_{i=1}^N \frac{1}{2} m v_i^2 \left[H(-x_i) H(x_i + v_i^x \Delta t) - H(x_i) H(-x_i - v_i^x \Delta t) \right]. \quad (3.8)$$

Finally, the third energy functional is the temperature of the gas extrapolated to the thermal wall boundaries

$$F_{3\pm}^e = \lim_{x \rightarrow \pm L/2} T(x). \quad (3.9)$$

The **temperature** is measured in cells as

$$T(x) = \frac{m \langle |\mathbf{v}_i|^2 \rangle - \langle v_i^x \rangle^2 - \langle v_i^y \rangle^2 - \langle v_i^z \rangle^2}{3k} \quad (3.10)$$

where the cell sum average is defined by equation (3.5) for steady state calculations and by (3.6) for transient calculations.

As with momentum and energy, the **diffusion of tagged particles** is measured by the functionals

$$F_{1\pm}^c = \frac{1}{A(k_f - k_i)\Delta t} \sum_{k=k_i}^{k_f} \sum_{i=1}^N \left[C_i' - C_i \right] H(-L/2 \pm (x_i + v_i^x \Delta t)) \quad (3.11)$$

and

$$F_2^c = \frac{1}{A(k_f - k_i)\Delta t} \sum_{k=k_i}^{k_f} \sum_{i=1}^N C_i \left[H(-x_i) H(x_i + v_i^x \Delta t) - H(x_i) H(-x_i - v_i^x \Delta t) \right] \quad (3.12)$$

which give the fluxes of tagged particles at the walls and in the center of the system, respectively.

The estimated **fractional truncation error** for some functional F is defined as

$$E(\Delta t) = \frac{|F(\Delta t) - F(\Delta t_0)|}{|F(\Delta t_0)|} \quad (3.13)$$

where Δt_0 is the reference time step. Ideally, one would wish to evaluate the exact error,

$$E_e(\Delta t) = \frac{|F(\Delta t) - F(0)|}{|F(0)|}.$$

Assuming the error is monotonic in Δt (e.g., $F(\Delta t) > F(\Delta t_0)$) then

$$E(\Delta t) = \frac{|F(0)|}{|F(\Delta t_0)|} \left[E_e(\Delta t) - E_e(\Delta t_0) \right] = E_e(\Delta t) \frac{|F(0)|}{|F(\Delta t_0)|} \left[1 - \frac{E_e(\Delta t_0)}{E_e(\Delta t)} \right].$$

Therefore $E(\Delta t)$ and $E_e(\Delta t)$ show the same convergence behaviour provided that $E_e(\Delta t_0)$ is sufficiently small compared with $E_e(\Delta t)$. For the results presented here $\Delta t_0 = \frac{1}{8}t_0$ and $\Delta t = \frac{1}{2}t_0, \dots, 16t_0$ so $\Delta t_0 \leq \frac{1}{4}\Delta t$, which is sufficient for our purposes.

The time step dependence of the transport coefficients may be predicted using **Green-Kubo analysis** (N. G. Hadjiconstantinou, "Analysis of discretization in the direct simulation Monte Carlo", *Phys. Fluids*, submitted, 1999). For the **viscosity**,

$$\eta = \eta_K \left(1 + \frac{32}{150\pi} \frac{\bar{v}_0^2 \Delta t^2}{\lambda_0^2} \right)$$

where η_K is the kinetic theory expression for the viscosity as given by Chapman-Enskog analysis. Similarly, for the **thermal conductivity**,

$$\kappa = \kappa_K \left(1 + \frac{64}{675\pi} \frac{\bar{v}_0^2 \Delta t^2}{\lambda_0^2} \right)$$

and **self-diffusion coefficient**,

$$D = D_K \left(1 + \frac{4}{27\pi} \frac{\bar{v}_0^2 \Delta t^2}{\lambda_0^2} \right).$$

Note that the results for viscosity and thermal conductivity are similar to those obtained by Green-Kubo analysis for the cell size dependence [2] with Δx replaced by $\bar{v}_0 \Delta t$. Interestingly, there is no corresponding cell size truncation error for the self-diffusion coefficient.

For weak gradients, the measured functionals are related to the transport coefficients as

$$E_{1+}^v(\Delta t) = E_{1-}^v(\Delta t) = E_2^v(\Delta t) = \frac{|\eta(\Delta t) - \eta(\Delta t_0)|}{|\eta(\Delta t_0)|} = \frac{32}{150\pi} \frac{\bar{v}_0^2 \Delta t^2}{\lambda_0^2} \quad (3.14)$$

$$E_{1+}^e(\Delta t) = E_{1-}^e(\Delta t) = E_2^e(\Delta t) = \frac{|\kappa(\Delta t) - \kappa(\Delta t_0)|}{|\kappa(\Delta t_0)|} = \frac{64}{675\pi} \frac{\bar{v}_0^2 \Delta t^2}{\lambda_0^2} \quad (3.15)$$

$$E_{1+}^c(\Delta t) = E_{1-}^c(\Delta t) = E_2^c(\Delta t) = \frac{|D(\Delta t) - D(\Delta t_0)|}{|D(\Delta t_0)|} = \frac{4}{27\pi} \frac{\bar{v}_0^2 \Delta t^2}{\lambda_0^2} \quad (3.16)$$

in the limit $\Delta t_0 \rightarrow 0$, $\Delta x \rightarrow 0$ and $N \rightarrow \infty$. As shown in the next section, the results from the simulations are in good agreement with these Green-Kubo predictions.

4. Simulation Results

This section presents the estimated truncation errors discussed in the previous section as measured in a variety of scenarios. For evaluating collisions and measuring statistical samples, the particles are sorted into cells of width Δx and cross-section A . For the results presented here, $L = 50\lambda_0$, $N = 50000$, and $\Delta x = \lambda_0/5$. Previous studies indicate that this cell size is sufficiently small [2] and the particle number sufficiently large [9], [8] that for our purposes the error with respect to Δx and N may be neglected. The numerical values of the physical quantities are scaled such that $m = 1$, $\lambda_0 = 1$, $T_0 = 1$, and $t_0 = 1$.

The following problems are considered (cf. Figure 1)

- (1) Steady state Couette flow with $u_{\pm}^y = \pm 0.2\bar{v}_0$, $T_{\pm} = T_0$, and $C_{\pm} = 0$;
- (2) Steady state Couette flow with $u_{\pm}^y = \pm \bar{v}_0$, $T_{\pm} = T_0$, and $C_{\pm} = 0$;
- (3) Transient Couette flow with $u_{\pm}^y = \pm \bar{v}_0$, $T_{\pm} = T_0$, and $C_{\pm} = 0$;
- (4) Steady state heat flow with $u_{\pm}^y = 0$, $T_- = 1.2T_0$, $T_+ = T_0$, and $C_{\pm} = 0$;
- (5) Steady state heat flow with $u_{\pm}^y = 0$, $T_- = 2T_0$, $T_+ = T_0$, and $C_{\pm} = 0$;
- (6) Transient heat flow with $u_{\pm}^y = 0$, $T_- = 3T_0$, $T_+ = T_0$, and $C_{\pm} = 0$;
- (7) Steady state tagged particle diffusion with $u_{\pm}^y = 0$, $T_{\pm} = T_0$, $C_- = 0$, and $C_+ = 0.1$.

For the **steady state scenarios** the system is initialized with a density, velocity and temperature near the steady state. The simulation is run for a time of $t_i = 25600t_0$ before statistical sampling initiates; samples are taken until the final time of $t_f = 102400t_0$. For comparison, the viscous relaxation time is

$$t_{\eta} = \frac{mn_0L^2}{2\eta_0} = \frac{8L^2}{5\sqrt{\pi}\lambda_0\bar{v}_0} \approx 2260t_0, \quad (4.1)$$

where η_0 is the viscosity at the reference state.

For the **transient runs** the gas is initialized to be at thermodynamic equilibrium with the reference temperature, constant density and average velocity zero. The simulation runs up to a stopping time of

$$t_S = 16t_0 \quad (4.2)$$

and a statistical sample is taken to measure the fluid velocity $u^y(x)$ and the temperature $T(x)$ (cf. (3.4), (3.10)). An ensemble of 10000 runs is performed and the samples from the ensemble are combined to compute $F_{3\pm}^v$ and $F_{3\pm}^e$ (cf. (3.3), (3.9)).

4.1. Steady state Couette flow (weak gradient)

The first scenario we consider is steady state Couette flow with a weak velocity gradient ($u_{\pm}^y = \pm 0.2\bar{v}_0$). Because the system is symmetric about $x = 0$, we define the averages (cf. (3.13), (3.1), (3.7))

$$E_1^v = \frac{E_{1+}^v + E_{1-}^v}{2}, \quad E_1^e = \frac{E_{1+}^e + E_{1-}^e}{2}. \quad (4.3)$$

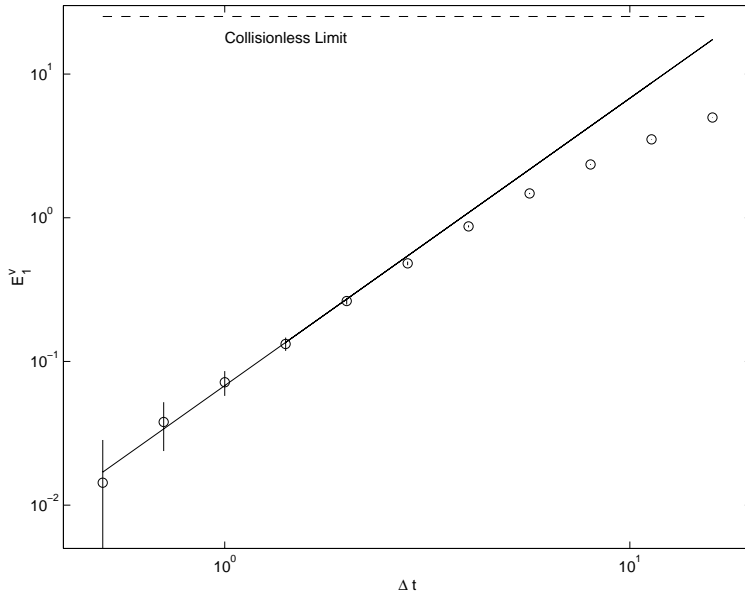


Figure 2: Estimated truncation error in the wall drag force, E_1^v , versus time step for steady state Couette flow. The solid line is given by equation (3.14) and the dashed line by equation (4.4).

Figures 2 and **3** show that the fractional truncation error in the drag force, E_1^v , and in the momentum flux, E_2^v , (cf. (3.13), (3.2)) go as Δt^2 except at the largest time steps. Moreover, the truncation error is in good quantitative agreement with equation (3.14).

The maximum error in the momentum transport is limited by the flux in the **collisionless limit**. In this limit the velocity distribution function is the sum of two half-Maxwellians with mean velocities u_{\pm}^y and temperatures T_{\pm} (see Appendix). For the momentum flux, one obtains

$$\tilde{F}_{1+}^v = \tilde{F}_{1-}^v = \tilde{F}_2^v = \frac{m}{2}(n_- u_-^y \bar{c}_- - n_+ u_+^y \bar{c}_+), \quad (4.4)$$

where

$$n_{\pm} = n_0 \frac{\sqrt{T_{\mp}}}{\sqrt{T_+} + \sqrt{T_-}}; \quad \bar{c}_{\pm} = \sqrt{\frac{8kT_{\pm}}{\pi m}} \quad (4.5)$$

are the number density and mean thermal speed for particles moving away from the wall located at $\pm L/2$. Figures 2 and 3 show that the truncation error deviates from equation (3.14) as the error saturates to the collisionless limit. Because the velocity gradient is weak the confidence intervals for the other measured errors (E_3^v and E_3^e) are too wide to establish conclusive results for the time step dependence.

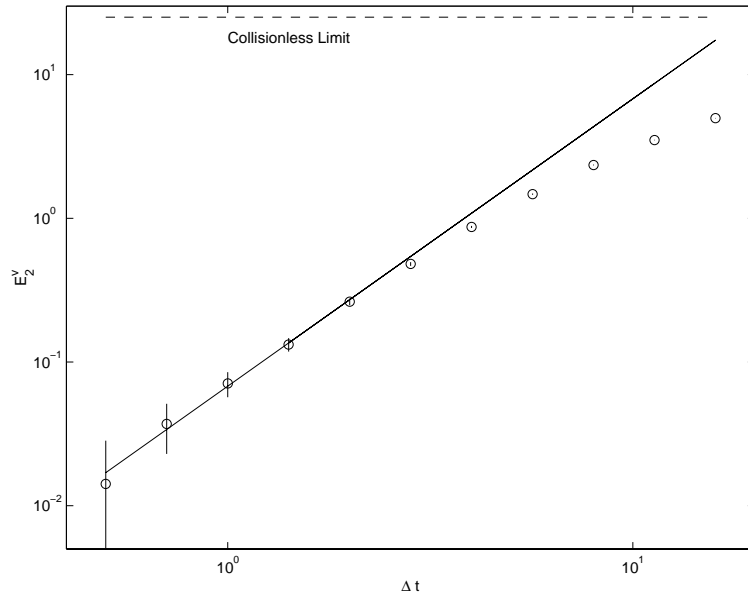


Figure 3: Estimated truncation error in the parallel momentum flux, E_2^v , versus time step for steady state Couette flow. The solid line is given by equation (3.14) and the dashed line by equation (4.4).

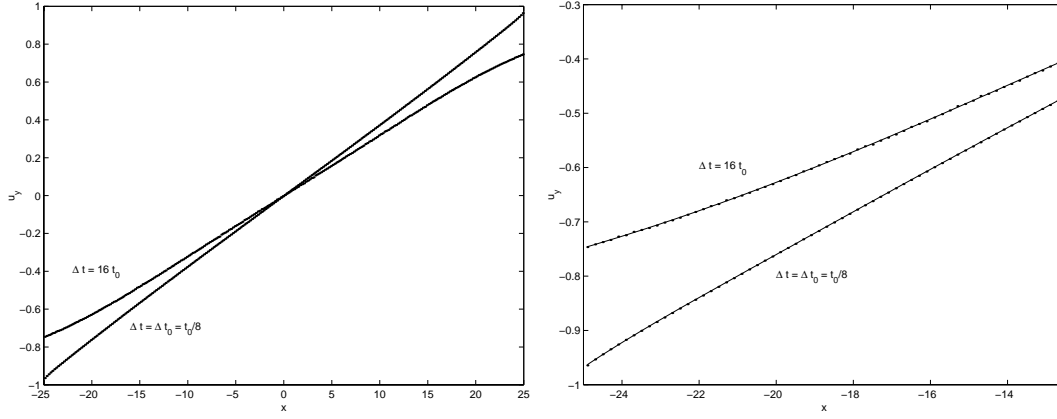


Figure 4: Fluid velocity, u_y , versus position for steady state Couette flow, as measured in the reference simulation ($\Delta t = \frac{1}{8}t_0$) and in the simulation with the largest time step ($\Delta t = 16t_0$). The left graph shows the entire velocity profile; the right graph shows the profile near the wall at $x = -L/2$ with the solid lines being the curve fits used to compute F_{3-}^v .

4.2. Steady state Couette flow (strong gradient)

Next we consider steady state Couette flow with a strong velocity gradient ($u_{\pm}^y = \pm \bar{v}_0$). The measured truncation errors E_1^v and E_2^v go as Δt^2 but the absolute error is about 20% larger than that predicted by equation (3.14).

Figures 4 and **5** show velocity and temperature profiles measured in the reference simulation ($\Delta t = \Delta t_0 = \frac{1}{8}t_0$) and in the simulation with the largest time step ($\Delta t = 16t_0$). In Couette flow the temperature is maximum in the center of the system due to viscous heating produced by the imposed shear. To evaluate $F_{3\pm}^v$ and $F_{3\pm}^e$ (cf. (3.3), (3.9)), these profiles were extrapolated to $x = \pm L/2$ by taking the data points between $x = \pm L/2$ and $\pm L/4$ and fitting them to a quartic polynomial.

Figures 6 and **7** show that the truncation error goes as Δt^2 except at the largest time steps. Again, since the system is symmetric about $x = 0$, we define the averages

$$E_3^v = \frac{1}{2}(E_{3+}^v + E_{3-}^v), \quad E_3^e = \frac{1}{2}(E_{3+}^e + E_{3-}^e). \quad (4.6)$$

In the **collisionless limit**, the velocity and temperature are

$$\tilde{u}^y = \frac{n_- u_-^y + n_+ u_+^y}{n_0} \quad (4.7)$$

and

$$\tilde{T} = \frac{n_- T_- + n_+ T_+}{n_0} + \frac{m}{3k} \frac{n_+ n_-}{n_0^2} (u_+^y - u_-^y)^2 \quad (4.8)$$

and independent of x . Figures 6 and 7 show that the truncation error saturates to the collisionless limit for large time steps.

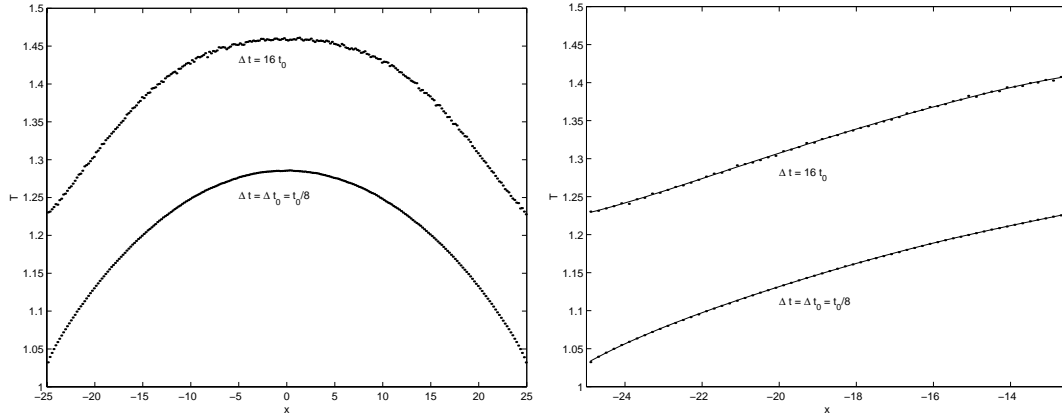


Figure 5: Temperature, T , versus position for steady state Couette flow, as measured in the reference simulation ($\Delta t = \frac{1}{8}t_0$) and in the simulation with the largest time step ($\Delta t = 16t_0$). The left graph shows the entire temperature profile; the right graph shows the profile near the wall at $x = -L/2$ with the solid lines being the curve fits used to compute F_{3-}^e .

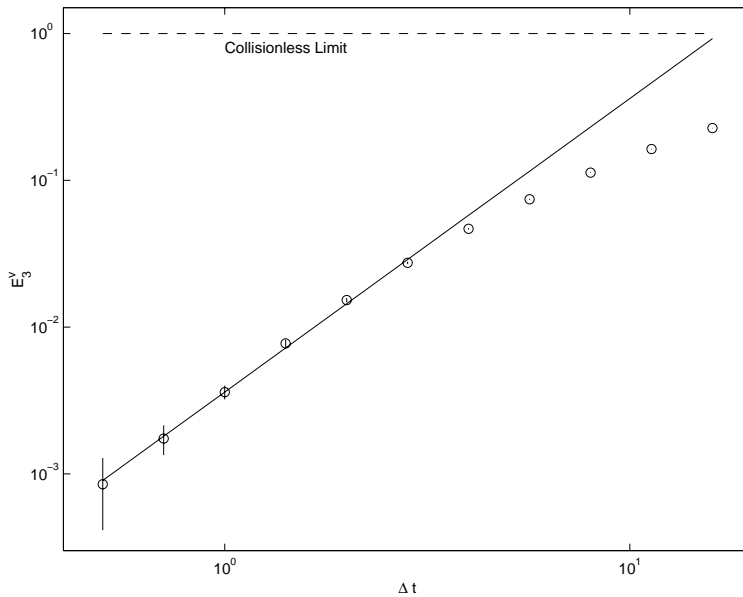


Figure 6: Estimated truncation error in the fluid velocity at the walls, E_3^v , versus time step for steady state Couette flow. The solid line has slope Δt^2 and the dashed line is obtained from equation (4.7).

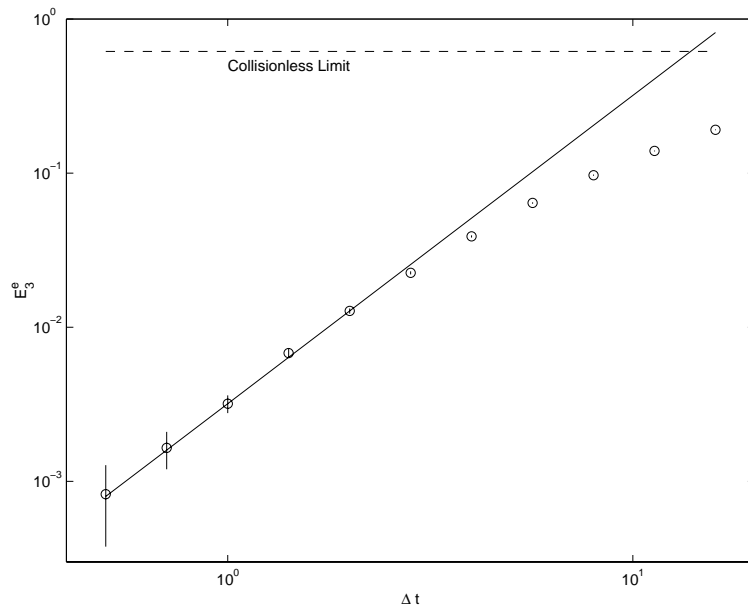


Figure 7: Estimated truncation error in the temperature at the walls, E_3^e , versus time step for steady state Couette flow. The solid line has slope Δt^2 and the dashed line is obtained from equation (4.8).

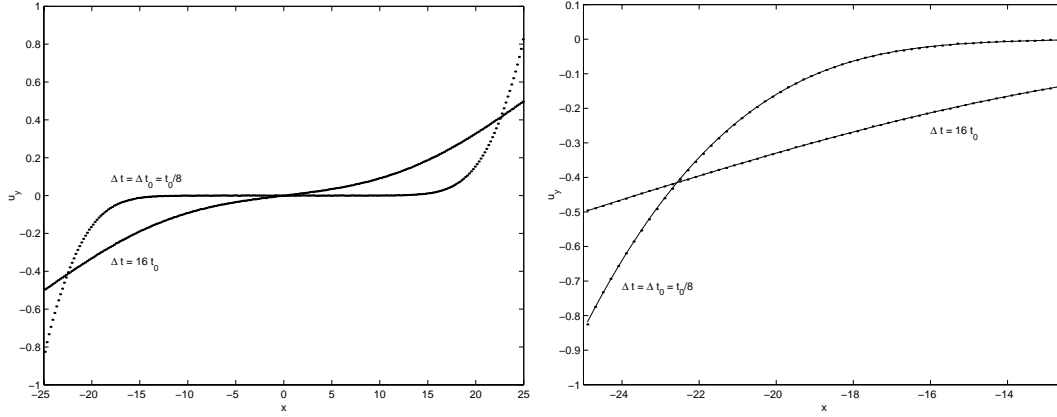


Figure 8: Fluid velocity u_y versus position for transient Couette flow, as measured in the reference simulation ($\Delta t = \frac{1}{8}t_0$) and in the simulation with the largest time step ($\Delta t = 16t_0$). The left graph shows the entire velocity profile; the right graph shows the profile near the wall at $x = -L/2$ with the solid lines being the curve fits used to compute F_{3-}^v .

4.3. Transient Couette flow

The third case we consider is transient Couette flow. **Figure 8** shows the velocity profiles measured in the reference simulation ($\Delta t = \Delta t_0 = \frac{1}{8}t_0$) and in the simulation with the largest time step ($\Delta t = 16t_0$). To evaluate $F_{3\pm}^v$ (cf. (3.3)), these profiles were extrapolated to $x = \pm L/2$ by taking the data points between $x = \pm L/2$ and $\pm L/4$ and fitting them to a quartic polynomial.

Figure 9 shows that the truncation error goes as Δt^2 except at the largest time steps. Again, since the system is symmetric about $x = 0$, we use the definition (4.6).

For the **collisionless limit**, for very long times ($t_S \gg t_\eta$) the velocity profile is given by equation (4.7). However, for the transient runs presented here we are interested in the short time behavior (cf. (4.1), (4.2), i.e. $t_S \ll t_\eta$) for which

$$\tilde{u}^y(\pm L/2) = \frac{1}{2}u_\pm^y. \quad (4.9)$$

In this situation equal numbers of particles are moving towards and away from each wall. The particles approaching a wall are distributed according to the equilibrium reference state while those leaving are thermalized with a wall's velocity and temperature. Figure 9 shows that the truncation error saturates to the collisionless limit for large time steps.

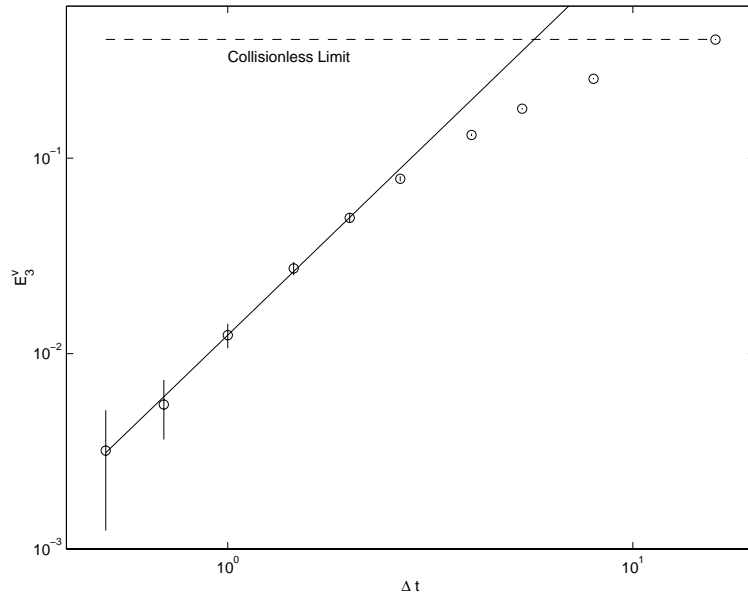


Figure 9: Estimated truncation error in the fluid velocity at the walls, E_3^v , versus time step for transient Couette flow. The solid line has slope Δt^2 and the dashed line is obtained from equation (4.9).

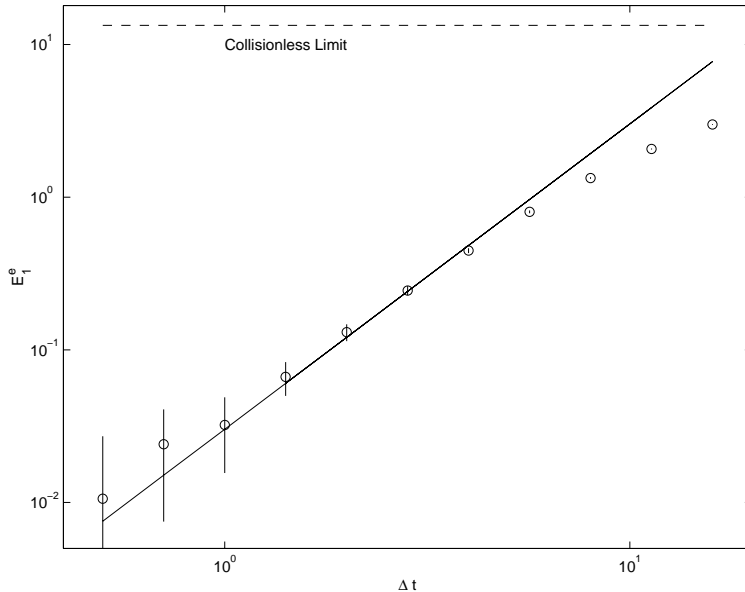


Figure 10: Estimated truncation error in the heat flux at the walls, E_1^e , versus time step for steady state heat flow. The solid line is given by equation (3.15) and the dashed line by equation (4.10).

4.4. Steady state heat flow (weak gradient)

In the next case we examine the walls are stationary but at different temperatures ($T_- = 1.2T_0$, $T_+ = T_0$) resulting in a heat flow. The system is *not* symmetric; though the temperature gradient is nearly linear there is a density gradient ($n \propto T^{-1}$) since at the steady state the pressure is constant.

The estimated truncation error E_1^e (cf. (4.3), (3.13), (3.7), (3.8)) versus time step is shown in **Figure 10**. Despite the asymmetry, we find that the difference between E_{1+}^e and E_{1-}^e is about an order of magnitude smaller than the confidence interval in their measurement so we only consider their average, E_1^e . Both E_1^e and E_2^e (shown in **Figure 11**) go as Δt^2 and are in good agreement with equation (3.15) except at the largest time steps where the heat flux is limited by the collisionless ceiling,

$$\tilde{F}_{1+}^e = \tilde{F}_{1-}^e = \tilde{F}_2^e = \frac{m\pi}{8}(n_- \bar{c}_-^3 - n_+ \bar{c}_+^3) + \frac{m}{4}(n_- \bar{c}_- u_-^{y^2} - n_+ \bar{c}_+ u_+^{y^2}). \quad (4.10)$$

Because the temperature gradient is weak the confidence intervals for error in the temperature at the wall ($E_{3\pm}^e$) are too wide to establish conclusively its time step dependence.

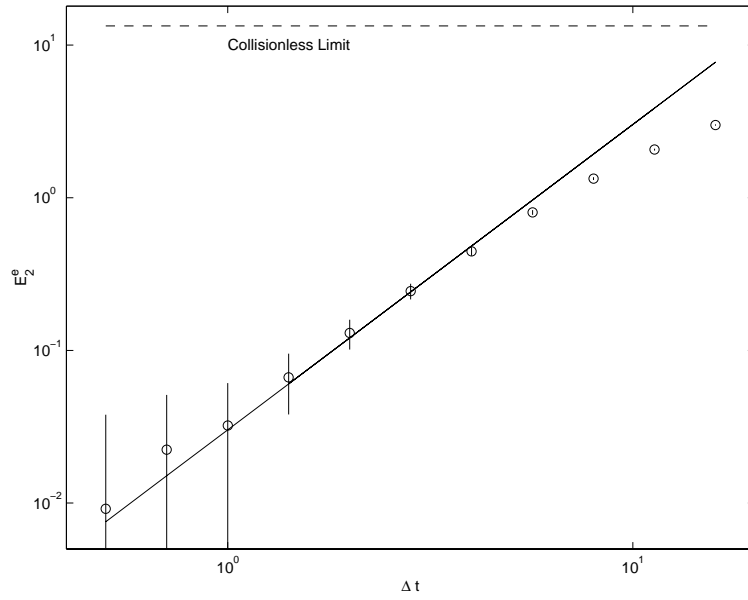


Figure 11: Estimated truncation error in the heat flux at the center, E_2^e , versus time step for steady state heat flow. The solid line is given by equation (3.15) and the dashed line by equation (4.10).

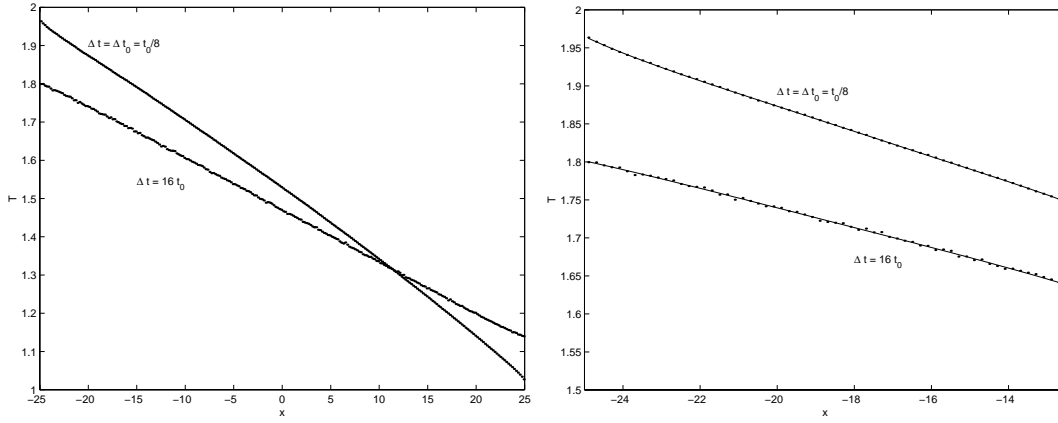


Figure 12: Temperature T versus position for steady state heat flow, as measured in the reference simulation ($\Delta t = \frac{1}{8}t_0$) and in the simulation with the largest time step ($\Delta t = 16t_0$). The solid lines in the left figure are the curve fits used to compute $F_{3\pm}^e$.

4.5. Steady state heat flow (strong gradient)

This case is similar to the previous one but with a larger temperature difference ($T_- = 2T_0$, $T_+ = T_0$). The measured truncation errors E_1^e and E_2^e go as Δt^2 but the absolute error is about 50% larger than that predicted by equation (3.15).

Figure 12 shows the temperature profiles measured in the reference simulation ($\Delta t = \Delta t_0 = \frac{1}{8}t_0$) and in the simulation with the largest time step ($\Delta t = 16t_0$). To evaluate $F_{3\pm}^e$, these temperature profiles were extrapolated to $x = \pm L/2$ by taking the data points between $x = \pm L/2$ and $\pm L/4$ and fitting them to a quartic polynomial.

Figure 13 shows that the truncation error goes as Δt^2 except at the largest time steps where the error saturates to the collisionless ceiling, as given by equation (4.8).

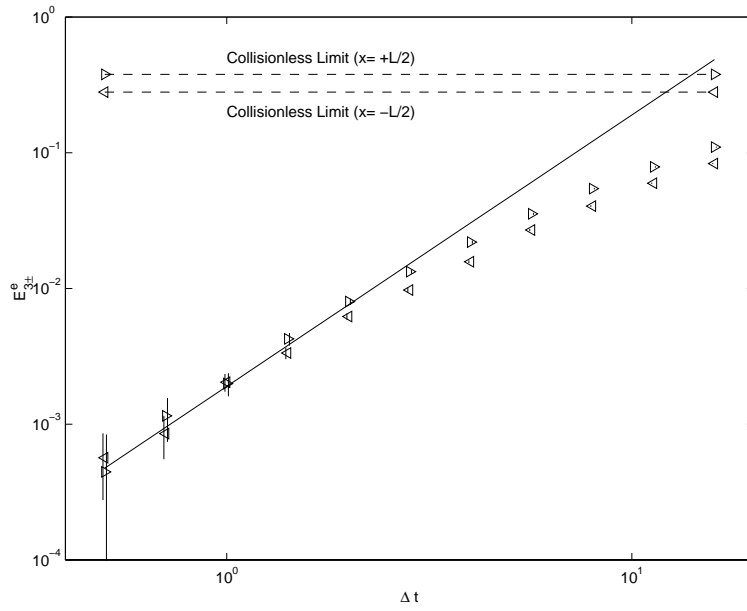


Figure 13: Estimated truncation error in the temperature at the walls, E_{3-}^e and E_{3+}^e (\triangleleft and \triangleright), versus time step for steady state heat flow. The solid line has slope Δt^2 and the dashed lines are obtained from equation (4.8).

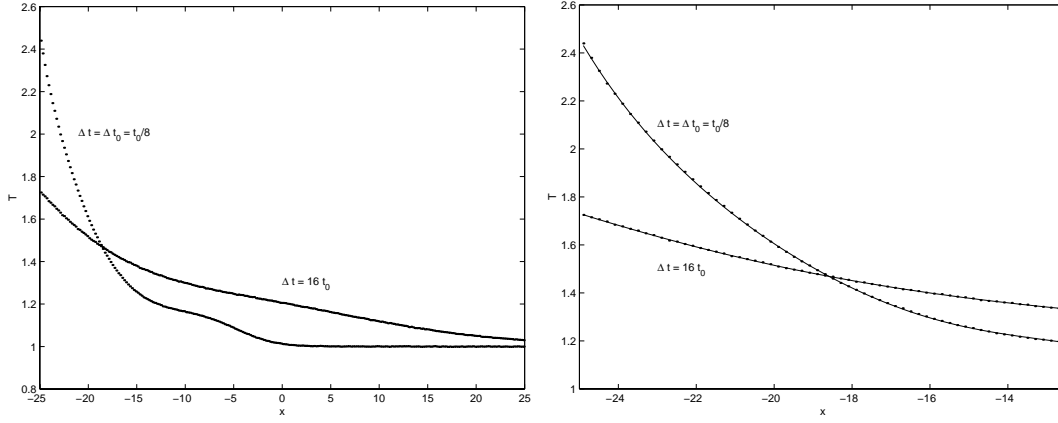


Figure 14: Temperature T versus position for transient heat flow, as measured in the reference simulation ($\Delta t = \frac{1}{8}t_0$) and in the simulation with the largest time step ($\Delta t = 16t_0$). The left graph shows the entire temperature profile; the right graph shows the profile near the wall at $x = -L/2$ with the solid lines being the curve fits used to compute F_{3-}^e .

4.6. Transient heat flow

The next case we consider is transient heat flow. **Figure 14** shows the temperature profiles measured in the reference simulation ($\Delta t = \Delta t_0 = \frac{1}{8}t_0$) and in the simulation with the largest time step ($\Delta t = 16t_0$). To evaluate F_{3-}^e (cf. (3.9)), these profiles were extrapolated to $x = -L/2$ by taking the data points between $x = -L/2$ and $-L/4$ and fitting them to a quartic polynomial.

Figure 15 shows that the truncation error goes as Δt^2 except at the largest time steps. Again, since the system is symmetric about $x = 0$, we use the definition (4.6). The **collisionless limit**, for short times ($t_S \ll t_\eta$), gives

$$\tilde{T}(-L/2) = \frac{n_-^* T_- + n_+^* T_0}{n_-^* + n_+^*} + \frac{m}{12k} \frac{n_+^* n_-^*}{(n_-^* + n_+^*)^2} (\bar{c}_- - \bar{c}_0)^2 \quad (4.11)$$

where

$$n_+^* = \frac{n_0}{2}; \quad n_-^* = \frac{n_0}{2} \sqrt{\frac{T_0}{T_-}}; \quad \bar{c}_0 = \sqrt{\frac{8kT_0}{\pi m}}. \quad (4.12)$$

Figure 15 shows that the truncation error saturates to the collisionless limit for large time steps.

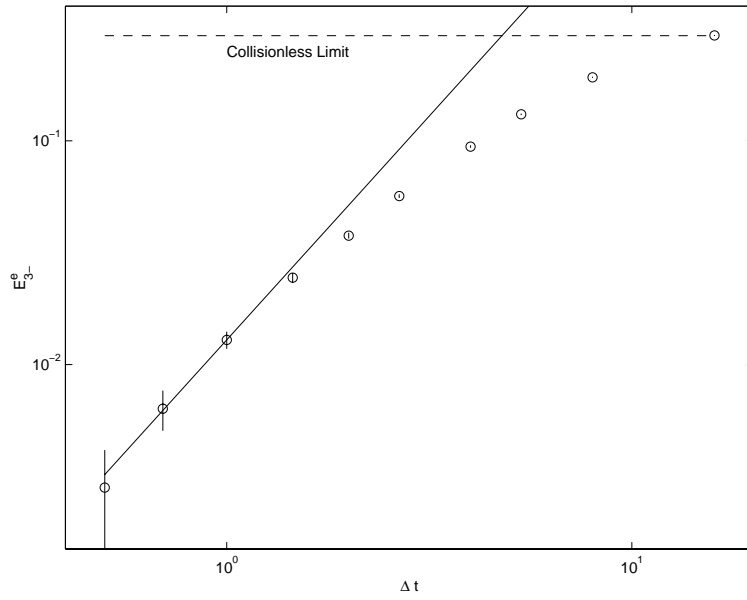


Figure 15: Estimated truncation error in the temperature at the walls, E_{3-}^e , versus time step for transient heat flow. The solid line has slope Δt^2 and the dashed line is obtained from equation (4.11).

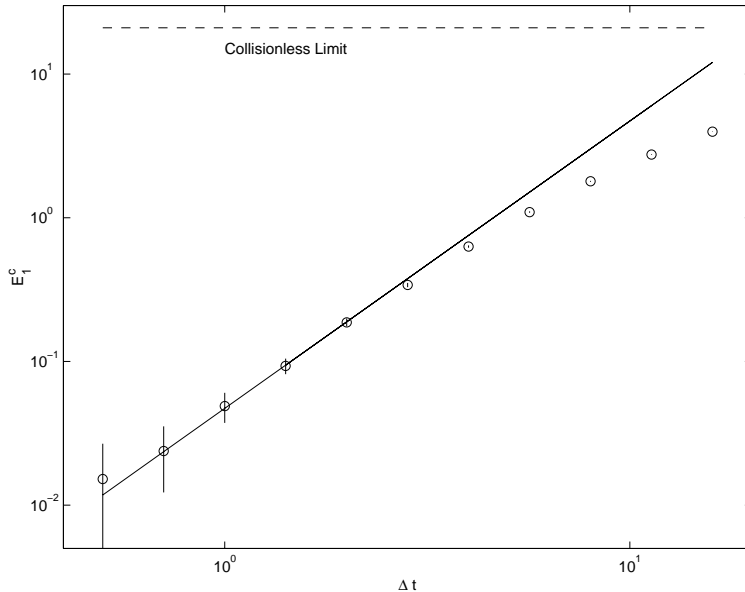


Figure 16: Estimated truncation error in the tagged particle flux at the walls, E_1^c , versus time step for steady state tagged particle diffusion. The solid line is given by equation (3.16) and the dashed line by equation (4.13).

4.7. Steady state tagged particle diffusion

The final scenario we consider is the diffusion of tagged particles. Specifically, ten percent of the particles that strike the left wall are tagged ($C_- = 0.1$); all particles striking the right wall are untagged ($C_+ = 0$). This gradient produces a diffusive flux of tagged particles. **Figures 16** and **17** show the two estimates for the truncation error in this flux, E_1^c and E_2^c , where $E_1^c = (E_{1-}^c + E_{1+}^c)/2$ (cf. (3.11), (3.12), (3.13)). The measured truncation error is in quantitative agreement with equation (3.16) except at the largest time steps where the flux saturates to the collisionless limit,

$$\tilde{F}_{1+}^c = \tilde{F}_{1-}^c = \tilde{F}_2^c = \frac{1}{2}(n_- \bar{c}_- C_- - n_+ \bar{c}_+ C_+) \quad (4.13)$$

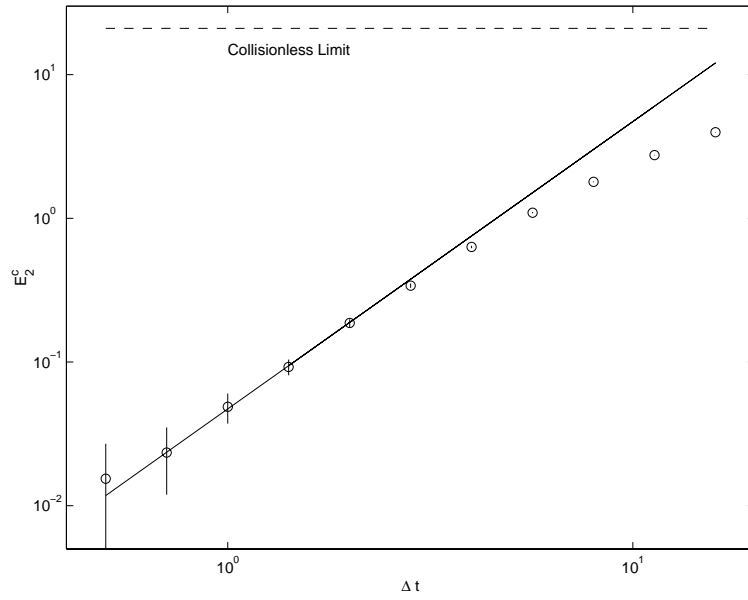


Figure 17: Estimated truncation error in the tagged particle flux at the center, E_2^c , versus time step for steady state tagged particle diffusion. The solid line is given by equation (3.16) and the dashed line by equation (4.13).

5. Concluding Remarks

The results from the previous section clearly indicate a time step error of order Δt^2 , when $\Delta t \rightarrow 0$. This is in agreement with the theoretical results from [5] outlined in Section 2. Note that consideration of a region near the collisionless limit, where Δt is still too big, may lead to wrong conclusions. Also the Green-Kubo predictions from Section 3 concerning the quantitative behaviour of the error in the transport coefficients have been confirmed.

In the variant proposed in [11], during a single iteration: particles move for a half time step; collisions are evaluated for a full time step; particles move again for a half time step; and statistical samples are measured. The accuracy of statistical samples taken between iteration points may improve because the sampling is time-centered. Otherwise, except for the first and last iteration, the global dynamics is equivalent to standard DSMC.

Our conclusions concerning the time step error apply both to the transient and the steady state situations. Corresponding analytical results for the steady state case, similar to those outlined in Section 2, would be of much interest. The problem of time step error seems to be closely linked to the occurrence of recollisions. More detailed studies are necessary to further clarify this connection.

Acknowledgments

The authors wish to thank F. Alexander, B. Alder, G. Bird, and N. Hadjiconstantinou for useful discussions. The work was supported in part by the Applied Mathematical Sciences Program of the DOE Office of Mathematics, Information, and Computational Sciences. One of the authors (AG) wishes to thank the Weierstrass Institute for Applied Analysis and Stochastics, where this research was initiated, for its hospitality during his stay in Berlin.

Appendix: Collisionless flow

In this appendix we derive expressions for hydrodynamic quantities (velocity, temperature, etc.) for a bimodal distribution of half-Maxwellians in the absence of collisions. Specifically, the combined distribution is taken as

$$nf = n_+ f_+ + n_- f_- \quad (\text{A.1})$$

where $n = n_+ + n_-$,

$$f_{\pm} = \frac{2\beta_{\pm}^3}{\pi^{3/2}} H(\mp \text{sign}(v^x)) \exp(-\beta_{\pm}^2(v^{x^2} + (v^y - u_{\pm}^y)^2 + v^{z^2})) \quad (\text{A.2})$$

and $\beta_{\pm} = \sqrt{m/2kT_{\pm}}$. Note that n_- is the number density of particles moving in the $+x$ -direction. The analysis here follows that in [4, Ch.7] with some minor generalizations.

The hydrodynamic variables are obtained by integration of moments of the distribution (A.1). We first state some useful general result. Consider arbitrary densities

$$f_0(v) = c f_1(v) + (1 - c) f_2(v), \quad v \in \mathcal{R}^3, \quad c \in [0, 1],$$

and denote

$$m_i = \int_{\mathcal{R}^3} v f_i(v) dv, \quad \sigma_i^2 = \int_{\mathcal{R}^3} \|v - m_i\|^2 f_i(v) dv, \quad i = 0, 1, 2.$$

Using the obvious properties

$$m_0 = c m_1 + (1 - c) m_2 \quad (\text{A.3})$$

and

$$\sigma_i^2 = \int_{\mathcal{R}^3} \|v\|^2 f_i(v) dv - \|m_i\|^2,$$

one obtains

$$\begin{aligned} \sigma_0^2 &= \int_{\mathcal{R}^3} \|v\|^2 f_0(v) dv - \|m_0\|^2 \\ &= c \sigma_1^2 + c \|m_1\|^2 + (1 - c) \sigma_2^2 + (1 - c) \|m_2\|^2 - \|m_0\|^2 \\ &= c \sigma_1^2 + (1 - c) \sigma_2^2 + c(1 - c) \|m_1\|^2 + (1 - c)c \|m_2\|^2 - 2c(1 - c) (m_1, m_2) \end{aligned}$$

so that

$$\sigma_0^2 = c \sigma_1^2 + (1 - c) \sigma_2^2 + c(1 - c) \|m_1 - m_2\|^2 \quad (\text{A.4})$$

follows.

From (A.3) one obtains the components of the **fluid velocity**, by symmetry, $u^x = \overline{v^x} = 0$ and $u^z = \overline{v^z} = 0$, while u^y (cf. (4.7)) is just the density weighted average of u_+^y and u_-^y . The translational **temperature** is defined as

$$T = \frac{m}{3k} \left(\overline{v^{x^2}} + \overline{v^{y^2}} + \overline{v^{z^2}} - \overline{v^x}^2 - \overline{v^y}^2 - \overline{v^z}^2 \right)$$

and, according to (A.4), takes the form (4.8) for the steady state case and (4.11) for the transient case. Notice that the temperature is increased by the relative velocity of the two Maxwellian streams since the variance of the distribution increases.

Next we consider the number, momentum and energy fluxes. For simplicity we evaluate the one-sided flux for one stream and compose the total flux at the last step of the calculation. The **number flux** for the particles moving in the $+x$ direction is (cf. (A.2))

$$\mathcal{F}_{n \rightarrow} = \int_0^\infty dv^x \int_{-\infty}^\infty dv^y \int_{-\infty}^\infty dv^z n_- f_- v^x = \frac{n_-}{\beta_- \sqrt{\pi}} = \frac{n_- \bar{c}_-}{2}.$$

Note that (cf. (4.5)) $1/\beta_\pm = \sqrt{2kT_\pm/m} = \bar{c}_\pm \sqrt{\pi}/2$. The net number flux is thus

$$\mathcal{F}_n = \mathcal{F}_{n \rightarrow} + \mathcal{F}_{n \leftarrow} = \frac{n_- \bar{c}_- - n_+ \bar{c}_+}{2}. \quad (\text{A.5})$$

from which we obtain equation (4.13). Similarly, for the y -component of the one-sided **momentum flux**,

$$\mathcal{F}_{v \rightarrow} = \int_0^\infty dv^x \int_{-\infty}^\infty dv^y \int_{-\infty}^\infty dv^z (mv^y) n_- f_- v^x = m u_-^y \mathcal{F}_{n \rightarrow}$$

from which we obtain the y -component of the net momentum flux, equation (4.4). Finally, the one-sided **energy flux** is

$$\begin{aligned} \mathcal{F}_{e \rightarrow} &= \int_0^\infty dv^x \int_{-\infty}^\infty dv^y \int_{-\infty}^\infty dv^z \left(\frac{1}{2} m v^2 \right) n_- f_- v^x \\ &= \frac{m}{2} \left[\frac{1}{\beta_-^2} + \left(\frac{1}{2\beta_-^2} + u_-^{y2} \right) + \frac{1}{2\beta_-^2} \right] \mathcal{F}_{n \rightarrow} = \frac{\pi m}{8} n_- \bar{c}_-^3 + \frac{m}{4} n_- \bar{c}_- u_-^{y2} \end{aligned}$$

from which we obtain the net energy flux, equation (4.10).

Up to this point the number density in each stream has been arbitrary. In the closed system shown in Figure 1, n_\pm is the number density of particles moving away from the thermal wall at $x = \pm L/2$. At the steady state the number flux of particles moving left and right must equal, so (A.5) gives $n_+ \bar{c}_+ = n_- \bar{c}_-$. Since $n_0 = n_+ + n_-$, we obtain (4.5). Note that the density is higher in the colder stream since the average speed is lower.

On the other hand, for the transient cases the particles approaching the walls are Maxwellian distributed at the reference density and temperature, n_0 and T_0 . For the wall at $x = -L/2$, the density approaching the wall is $n_+^* = \frac{1}{2} n_0$. Since the total number flux at the wall must be zero, (A.5) gives $n_-^* = n_+^* \bar{c}_0 / \bar{c}_-$ from which we obtain (4.12).

References

- [1] F. J. Alexander and A. L. Garcia. The direct simulation Monte Carlo method. *Computers in Physics*, 11(6):588–593, 1997.
- [2] F. J. Alexander, A. L. Garcia, and B. J. Alder. Cell size dependence of transport coefficients in stochastic particle algorithms. *Phys. Fluids*, 10(6):1540–1542, 1998.
- [3] H. Babovsky and R. Illner. A convergence proof for Nanbu’s simulation method for the full Boltzmann equation. *SIAM J. Numer. Anal.*, 26(1):45–65, 1989.
- [4] G. A. Bird. *Molecular Gas Dynamics and the Direct Simulation of Gas Flows*. Clarendon Press, Oxford, 1994.
- [5] S. V. Bogomolov. Convergence of the method of summary approximation for the Boltzmann equation. *U.S.S.R. Comput. Math. and Math. Phys.*, 28(1):79–84, 1988.
- [6] S. Caprino, M. Pulvirenti, and W. Wagner. Stationary particle systems approximating stationary solutions to the Boltzmann equation. *SIAM J. Math. Anal.*, 29(4):913–934, 1998.
- [7] C. Cercignani, R. Illner, and M. Pulvirenti. *The Mathematical Theory of Dilute Gases*. Springer, New York, 1994.
- [8] G. Chen and I. D. Boyd. Statistical error analysis for the direct simulation Monte Carlo technique. *J. Comput. Phys.*, 126:434–448, 1996.
- [9] M. A. Fallavollita, D. Baganoff, and J. D. McDonald. Reduction of simulation cost and error for particle simulations of rarefied flows. *J. Comput. Phys.*, 109(1):30–36, 1993.
- [10] R. Illner. Approximation methods for the Boltzmann equation. In B. D. Shizgal and D. P. Weaver, editors, *Rarefied Gas Dynamics: Theory and Simulations*, volume 159 of *Progress in Astronautics and Aeronautics*, pages 551–564. AIAA, Washington, DC, 1994.
- [11] T. Ohwada. Higher order approximation methods for the Boltzmann equation. *J. Comput. Phys.*, 139:1–14, 1998.
- [12] W. Wagner. A convergence proof for Bird’s direct simulation Monte Carlo method for the Boltzmann equation. *J. Statist. Phys.*, 66(3/4):1011–1044, 1992.
- [13] W. Wagner. Theoretical comparison of stochastic particle methods in rarefied gas dynamics. In B. D. Shizgal and D. P. Weaver, editors, *Rarefied Gas Dynamics: Theory and Simulations*, volume 159 of *Progress in Astronautics and Aeronautics*, pages 353–360. AIAA, Washington, DC, 1994.